Low-Frequency Pycnocline Variability in the Northeast Pacific

ANTONIETTA CAPOTONDI AND MICHAEL A. ALEXANDER
NOAA/CIRES Climate Diagnostics Center, Boulder, Colorado

CLARA DESER
National Center for Atmospheric Research, Boulder, Colorado*

ARTHUR J. MILLER
Scripps Institution of Oceanography, La Jolla, California

(Manuscript received 14 January 2004, in final form 23 November 2004)

ABSTRACT

The output from an ocean general circulation model (OGCM) driven by observed surface forcing is used in conjunction with simpler dynamical models to examine the physical mechanisms responsible for interannual to interdecadal pycnocline variability in the northeast Pacific Ocean during 1958–97, a period that includes the 1976–77 climate shift. After 1977 the pycnocline deepened in a broad band along the coast and shoaled in the central part of the Gulf of Alaska. The changes in pycnocline depth diagnosed from the model are in agreement with the pycnocline depth changes observed at two ocean stations in different areas of the Gulf of Alaska. A simple Ekman pumping model with linear damping explains a large fraction of pycnocline variability in the OGCM. The fit of the simple model to the OGCM is maximized in the central part of the Gulf of Alaska, where the pycnocline variability produced by the simple model can account for ~70%–90% of the pycnocline depth variance in the OGCM. Evidence of westward-propagating Rossby waves is found in the OGCM, but they are not the dominant signal. On the contrary, large-scale pycnocline depth anomalies have primarily a standing character, thus explaining the success of the local Ekman pumping model. The agreement between the Ekman pumping model and OGCM deteriorates in a large band along the coast, where propagating disturbances within the pycnocline, due to either mean flow advection or boundary waves, appear to play an important role in pycnocline variability. Coastal propagation of pycnocline depth anomalies is especially relevant in the western part of the Gulf of Alaska, where local Ekman pumping-induced changes are anticorrelated with the OGCM pycnocline depth variations. The pycnocline depth changes associated with the 1976–77 climate regime shift do not seem to be consistent with Sverdrup dynamics, raising questions about the nature of the adjustment of the Alaska Gyre to low-frequency wind stress variability.

1. Introduction

The oceanic pycnocline, a subsurface layer characterized by large vertical density gradients, can be viewed as the interface between the surface ocean mixed layer and the deep ocean. Changes in pycnocline depth may be indicative of changes in upwelling, a process that influences the exchange of properties between the deep and upper ocean. Large areas of the northeast Pacific Ocean are characterized by a fresh and well-mixed surface layer, separated from the deeper ocean by large salinity gradients, or halocline. At high latitudes, where temperatures are low, salinity has a dominant influence on density, particularly in winter, so that pycnocline depth is very similar to winter mixed layer depth (Freeland et al. 1997). Thus, understanding the processes governing pycnocline variability can also help understand the changes in mixed layer depth, a quantity that has a large influence upon biological productivity (Polovina et al. 1995; Gargett 1997).

What processes control pycnocline depth variability

* The National Center for Atmospheric Research is sponsored by the National Science Foundation.

Corresponding author address: Antonietta Capotondi, NOAA/CIRES Climate Diagnostics Center, R/CDC1, 325 Broadway, Boulder, CO 80305-3328.
E-mail: Antonietta.Capotondi@noaa.gov

in the northeast Pacific? Using subsurface observations over the period 1968–90, Lagerloef (1995) examined interannual and decadal variations of the dynamic height field, which is closely related to pycnocline topography, over the Gulf of Alaska. The dominant mode of variability of the dynamic height field, identified through empirical orthogonal function (EOF) analysis, captured the 1976–77 climate shift and was well correlated with other climate indices. A simple model for the evolution of the dynamic height field, in which the forcing was supplied by the local Ekman pumping, and dissipation was modeled with a linear damping term, appeared to reproduce a large fraction of the low-frequency dynamic topography variations. However, the hindcast of dynamic heights underestimated the observed variability in the western half of the gyre, a result that Lagerloef (1995) attributed to the presence of westward propagating baroclinic Rossby waves.

Cummins and Lagerloef (2002, CL02 hereinafter) used the same Ekman pumping model described by Lagerloef (1995) to examine the structure of pycnocline depth variability forced by the dominant patterns of anomalous Ekman pumping over the northeast Pacific (30°–60°N, 180°–120°W) during 1948–2000. The evolution of pycnocline depth predicted by the simple Ekman pumping model reproduced well the observed variations at Ocean Weather Station Papa (OWS P: 50°N, 145°W). However, CL02 were unable to test the performance of the simple model at other locations in the Gulf of Alaska and to verify the accuracy of the spatial patterns of pycnocline depth changes produced by the model over the entire northeast Pacific. Cummins and Lagerloef (2004, CL04 hereinafter) further investigated the performance of the local Ekman pumping model of CL02, by estimating its ability to reproduce observed SSH variability in the northeast Pacific during 1993–2003, and concluded that interannual variability in the Gulf of Alaska is dominated by the local response to wind forcing.

The success of the simple Ekman pumping model in explaining pycnocline variability is somewhat surprising given the role of Rossby waves in the adjustment of the large-scale ocean circulation to changes in surface forcing. Indeed, satellite altimetry shows westward-propagating sea surface height (SSH) anomalies in the northeast Pacific (Kelly et al. 1993; Fu and Qiu 2002). Further, Qiu (2002) has shown that SSH variability from the Ocean Topography Experiment (TOPEX)/Poseidon (T/P) altimeter mission (1993–2001), areally averaged over the offshore region of the Gulf of Alaska, can be largely explained by first-mode baroclinic Rossby wave propagation.

The simplest dynamical paradigm to describe the steady-state response of the large-scale ocean circulation to wind forcing is the Sverdrup relation (Sverdrup 1947), which expresses the linear vorticity balance between wind stress curl and meridional advection of planetary vorticity. Although the Sverdrup relation was originally derived as a theory for the steady-state ocean circulation, it has proven very useful to explain circulation changes associated with large-scale variations of the wind forcing. Deser et al. (1999) have related the intensification of the Kuroshio Extension after the mid-1970s to the strengthening of the westerlies in the central Pacific using Sverdrup dynamics. In the Gulf of Alaska, the Alaskan Stream can be viewed as the western boundary current of the Alaska gyre, and it is conceivable that some of the changes in the upper-ocean density structure and circulation associated with the 1976–77 climate shift can be explained in terms of Sverdrup dynamics. Qiu (2002) has interpreted the annual modulation of the Alaska gyre intensity during 1993–2000 in terms of time-dependent Sverdrup balance. However, the dynamical balances governing the variations of the Alaska gyre at decadal time scales are still unclear.

In this study we examine the physical mechanisms responsible for low-frequency (interannual to interdecadal) pycnocline variability in the northeast Pacific during 1958–97. Both interannual and decadal time scales will be examined, but our major focus will be on the decadal–interdecadal variations and, in particular, those associated with the 1976–77 climate shift. The specific questions we ask are: What fraction of pycnocline variability can be explained by local Ekman pumping in different areas of the Gulf of Alaska? If the simple model of CL02 and CL04 fails in some areas, what other processes control pycnocline changes in those areas? What is the role of baroclinic Rossby waves in pycnocline variability? Does Sverdrup balance hold at decadal time scales? To answer these questions we will use the output from an ocean general circulation model (OGCM) driven by observed surface forcing. After testing the model's performance at locations where long-term observations are available, the OGCM output is used to test the different dynamical hypotheses. Our study will extend the work of CL02 by testing the local Ekman pumping model over the entire northeast Pacific. It will also extend and complement the work of CL04 by examining the changes that took place across the mid-1970s.

The OGCM used for this study is described in section 2, and in section 3 the performance of the OGCM is examined by comparing the pycnocline depth changes in the OGCM with those observed at two oceanographic stations in different areas of the Gulf of Alaska.

The influence of local Ekman pumping upon pycnocline variability is examined in section 4, and in section 5 the role of baroclinic Rossby waves is considered. The validity of the Sverdrup balance at decadal time scales is examined in section 6, and the processes governing the evolution of pycnocline depth anomalies along the coast is analyzed in section 7. We conclude in section 8.

2. The OGCM

The OGCM used for this study is the National Center for Atmospheric Research ocean model (NCOM) that has been described in detail by Large et al. (1997), Gent et al. (1998), and Large et al. (2001). The specific numerical simulation analyzed here is described in Doney et al. (2003). In this section we only provide a brief summary of the basic model characteristics and information about the surface forcing used for this simulation.

NCOM is derived from the Geophysical Fluid Dynamics Laboratory (GFDL) Modular Ocean Model with the addition of a mesoscale eddy flux parameterization along isopycnal surfaces (Gent and McWilliams 1990) and a nonlocal planetary boundary layer parameterization (Large et al. 1994). The model is global, with a horizontal resolution of 2.4° in longitude and varying resolution in latitude ranging from 0.6° near the equator to 1.2° at high latitudes. The model version used for this study includes an anisotropic viscosity parameterization (Large et al. 2001) with enhanced viscosity close to ocean boundaries and much weaker viscosity in the ocean interior.

The surface forcing includes momentum, heat, and freshwater fluxes for the period 1958–97. The wind stress is computed from the reanalyses fields produced at the National Centers for Environmental Prediction (NCEP) (Kalnay et al. 1996) using bulk formulas. The sensible and latent heat fluxes are computed from the NCEP winds and relative humidity and the model's SSTs using standard air–sea transfer equations (Large and Pond 1982; Large et al. 1997). Sensible and latent heat fluxes depend on the difference between SST and surface air temperature. Since SST and air temperature closely track each other, when observed air temperatures are used in the bulk formulas, as in the present model simulation, the model's SST is relaxed toward observations (Haney 1971). The relaxation time scale is relatively short (30–60 days for typical mixed layer depths), so the SST in the model can be expected to be strongly constrained by the surface forcing rather than by the interior ocean dynamics.

The numerical simulation is started from an initial condition obtained from a preliminary climatological integration, so the initial model state is not too different from the mean state characteristic of the 40-yr experiment. Then the model was run for two 40-yr cycles, the second cycle starting from the conditions achieved at the end of the first 40-yr segment. The mismatch between the model state and the forcing at the beginning of the second cycle did not seem to produce any long-term transient behavior, but some residual drift in temperature and salinity can be detected at depths larger than approximately 500 m (Doney et al. 2003). Here we analyze the output for the second 40-yr period using monthly mean values.

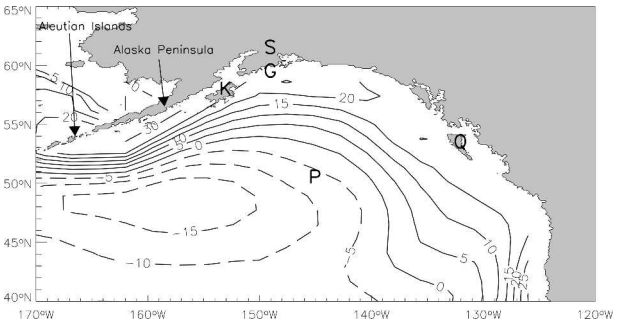

FIG. 1. Pycnocline depth changes associated with the 1976–77 climate regime shift from the output of the NCAR OGCM. The depth of the 26.4 σ_θ isopycnal is used as proxy for pycnocline depth. The positions of OWS P (P: 50°N, 145°W) and GAK1 (G: 59°N, 149°W) and the location of Kodiak Island (K), Seward (S), Queen Charlotte Island (Q), the Alaska Peninsula, and the Aleutian Islands are indicated for reference.

3. How realistic is pycnocline variability in the OGCM?

Lagerloef (1995) has shown that a significant fraction (28%) of the subsurface variance over the period 1960–90 is associated with the 1976–77 climate regime shift. Thus, we start by examining the pycnocline depth variations exhibited by the OGCM in association with the 1976–77 climate shift. The depth of the 26.4 σ_θ isopycnal, which lies in the core of the main pycnocline, is used as proxy for pycnocline depth. The mean depth of the 26.4 σ_θ isopycnal ranges from ~100 m in the center of the Alaska gyre to 150–180 m around the rim of the gyre. The changes in pycnocline depth are computed as the difference between the pycnocline depth in the period 1977–97 (period 2) and the pycnocline depth in the period 1960–75 (period 1). After the mid-1970s, the pycnocline was shallower in the central part of the Gulf of Alaska and deeper in a broad band following the coast (Fig. 1). The deepening was more pronounced in the western part of the Gulf of Alaska, to the southwest of Kodiak Island (K in Fig. 1), following approximately the Alaska Peninsula. A similar pattern of pycnocline changes was found by Miller et al. (1994) in a coarser-resolution (~4°) ocean model hindcast, using surface

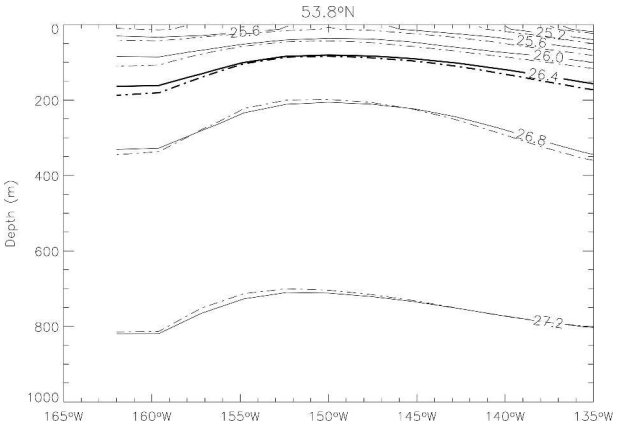

FIG. 2. Zonal section of mean potential density along 53.8°N for the periods 1958–75 (solid contours) and 1977–97 (dot–dashed contours). Contour interval is 0.4 σ_θ units. The 26.4 σ_θ isopycnal, used as proxy for pycnocline depth, is highlighted with a thick contour for both periods.

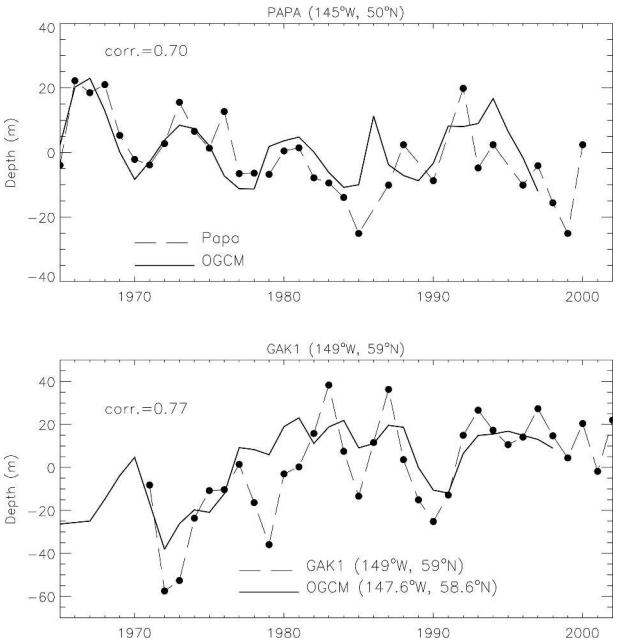

FIG. 3. Pycnocline depth variations (m) at (top) OWS P and (bottom) Station GAK1. Positive anomalies indicate deeper pycnocline, while negative anomalies correspond to a shallower pycnocline. The dots connected by the dashed line are the winter averages of observed values at the two stations (usually a few values for each winter), while the solid line shows the winter pycnocline depth anomalies from the NCAR OGCM, based on monthly averages. Correlation coefficients between the observed and modeled winter values are 0.7 and 0.77 at Papa and GAK1, respectively. The observed time series at Papa was kindly provided by P. Cummins.

forcing fields from the COADS dataset instead of NCEP. The leading mode of a simple stochastic model forced by Ekman pumping also displayed the spatial structure and temporal evolution characteristics of the 1976–77 regime shift (Fig. 4 in CL02). Changes in the density structure are detectable to depths greater than ~800 m, but appear to be more pronounced in the upper ocean as shown by a zonal density section along 53.8°N (Fig. 2). Above 400 m, the isopycnals deepen toward the eastern and western edges of the gyre after the mid-1970s, resulting in a more pronounced doming of the density structure.

Is the pattern of pycnocline variations in Fig. 1 realistic? Subsurface observations are generally sparse and salinity data in particular are very limited. Since salinity is an important factor controlling the potential density distribution in the subarctic Pacific, the paucity of salinity data limits the possibility of testing the performance of the OGCM over the whole northeast Pacific. However, there are a few oceanographic stations in the Gulf of Alaska where measurements of both temperature and salinity are available over a long period of time including the 1976–77 climate shift. We will use measurements from two stations, Ocean Weather Station Papa (OWS P, P in Fig. 1), which is located in the area where the pycnocline becomes shallower, and station GAK1 (G in Fig. 1), which is in the band where the pycnocline deepens.

OWS P (50°N, 145°W) provides a long record of bottle cast and CTD data over the period 1957–94. The time series has been recently augmented by more recent observations from 1995 to 1999. Generally, the density of observations is higher in the earlier period, 1957–81, when OWS P was occupied on a regular basis by a weather ship. Freeland et al. (1997) have computed pycnocline depths by assuming a two-layer representation of the density structure and using a least squares approach to determine the thickness of the upper layer from the observed density profiles. The two-layer representation is appropriate for wintertime (December–April) conditions, and it tracks the core of the main pycnocline in winter. CL02 have used the additional observations after 1994 to extend the time series of mean winter pycnocline depth from 1994 to 1999. Thus, the whole time series covers the period 1957–99, with gaps in 1985, 1988, 1990, and 1994. The resulting time series is compared in Fig. 3a with the winter pycnocline depth from the OGCM. The correlation between the two time series is 0.7, and the amplitude of the OGCM pycnocline depth anomalies is also approximately correct (the standard deviation of the OGCM time series is 9.7 m and the observed time series standard deviation is 11.3 m). Notice that the observed pycnocline depth anomaly values are often averages of few data over the winter months, while the winter pycnocline depths estimated from the OGCM are based on monthly aver-

ages of potential density, which is available at each model time step (of the order of one day). Thus, higher-frequency processes (e.g., mesoscale eddies and baroclinic tides), which are filtered out in the OGCM, may contribute to some of the observed pycnocline variability. Both model and observations indicate a shoaling trend of the main pycnocline, as discussed by Freeland et al. (1997) and CL02.

Station GAK1 (59°N, 149°W) is located at the mouth of Resurrection Bay near Seward, Alaska, where the OGCM indicates a deepening of the pycnocline after the mid-1970s (Fig. 1). Profiles of temperature and salinity to a depth of 250 m have been measured starting in December 1970, and are still ongoing. The number of observations over the winter period varies from less than 5 measurements in 1972, 1980, 1981, and 1985 to a maximum of 15 values in 1999. Starting from the individual density profiles, we have estimated the depth of the 25.4 σ_θ isopycnal, which is located close to the base of the observed winter pycnocline. Winter values have then been computed by averaging all the values between December and April. Standard deviations about each winter value (not shown) can be as large as 50 m. Station GAK1 is situated very close to shore, and there is no model grid point available at the exact location of the station. So we have estimated winter pycnocline depths from the OGCM at the closest model grid point (58.6°N, 147.6°W). The comparison between the observed and simulated depth anomalies is shown in Fig. 3b. Although the observed time series exhibits interannual fluctuations of larger amplitude than the time series from the OGCM, which are based on monthly averages of values at each model time step, the two time series agree quite well (the correlation coefficient is 0.77) on both interannual and longer time scales (apart from a discrepancy in 1979–81). In particular, the low-frequency behavior is very similar in both time series and indicates a deepening of the pycnocline after the mid-1970s. Thus, the comparison with observations indicates that the pattern of pycnocline depth changes produced by the OGCM is believable. Next we use the OGCM to assess which fraction of the pycnocline variability can be explained by local Ekman pumping.

4. Where is Ekman pumping important?

The vertical velocity at the base of the Ekman layer due to the divergence of the Ekman currents (Ekman pumping) is defined as the vertical component of the curl of the wind stress $\boldsymbol{\tau}$ divided by the Coriolis parameter f and the mean density of seawater ρ_o:

$$W_E = \left[\nabla \times \left(\frac{\boldsymbol{\tau}}{\rho_0 f}\right)\right]_z. \quad (1)$$

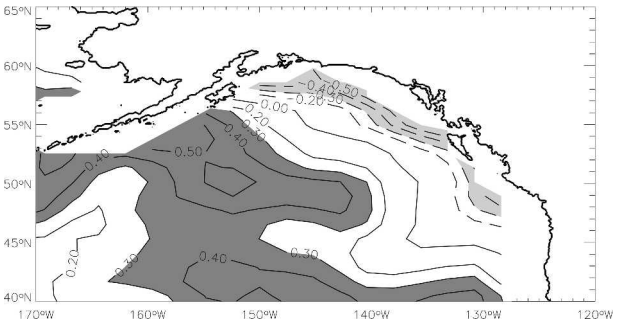

FIG. 4. Winter Ekman pumping changes associated with the 1976–77 climate regime shift. Contour interval is 0.1×10^{-4} cm s^{-1}. Solid contours indicate positive values, while dashed contours are used for negative values. Anomalies larger than 0.3×10^{-4} cm s^{-1} are dark shaded, while values smaller than -0.3×10^{-4} cm s^{-1} are light shaded. The mean Ekman pumping is positive over the Gulf of Alaska. Negative Ekman pumping anomalies imply reduced upwelling and vice versa.

The changes in the Ekman pumping field associated with the 1976–77 climate shift are shown in Fig. 4 as the difference between Ekman pumping during winter (December–April) in 1977–97 (period 2) and 1960–75 (period 1). The resulting pattern shows negative W_E changes (anomalous downwelling) in a broad band that follows the coast to the east of Kodiak Island (indicated with a K in Fig. 1), and positive changes (anomalous upwelling) elsewhere in the Gulf of Alaska, with maximum values extending to the southeast of the Alaskan Peninsula. The largest negative difference is achieved in the very northern part of the Gulf of Alaska, between approximately Seward (S in Fig. 1) and Queen Charlotte Island (Q in Fig. 1). Since the time-averaged Ekman pumping is positive (e.g., upwelling) over the whole Gulf of Alaska, a positive (negative) difference implies that upwelling is enhanced (diminished) after the 1976–77 climate shift. The pattern of W_E changes in Fig. 4 is very similar to that computed by Lagerloef (1995) using an empirical orthogonal function approach.

The pattern of W_E bears some similarity to the distribution of pycnocline changes in Fig. 1: areas of negative (positive) W_E differences generally correspond to areas of deeper (shallower) pycnocline after 1977. The major discrepancy between the two fields occurs in the coastal band extending southwestward from Kodiak Island to the Aleutian Islands, where a positive change in W_E from period 1 to period 2 is associated with a deeper pycnocline. The local correlation between Ekman pumping and pycnocline depth from the OGCM (h_{OGCM}) is shown in Fig. 5a using low-pass filtered Ekman pumping data to remove periods shorter than 2 yr and finding the lag at which the correlation is maxi-

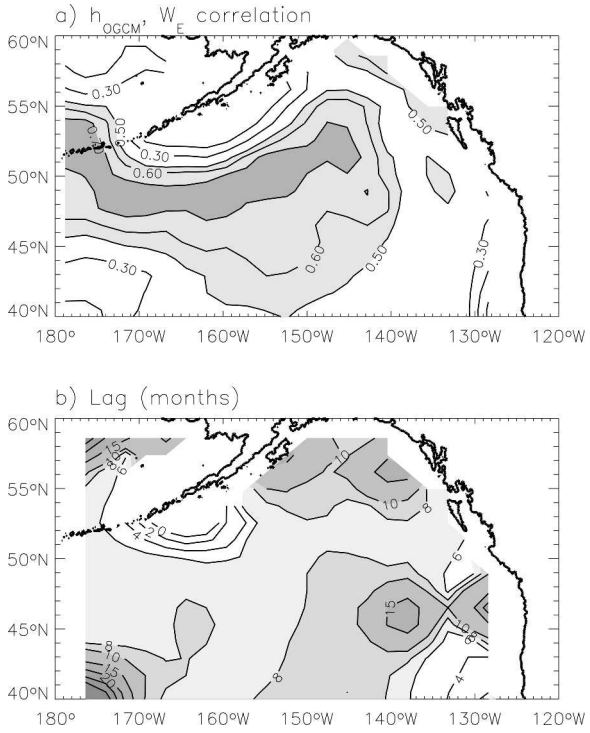

FIG. 5. (a) Maximum lag correlations between low-pass filtered Ekman pumping (periods shorter than 2 yr are removed) and pycnocline depth anomalies. Pycnocline depth anomalies have been multiplied by −1 to achieve positive correlations (a positive depth anomaly indicates deeper pycnocline, and should be associated with negative W_E anomalies, and vice versa). Values larger than 0.5 are light shaded, while values larger than 0.7 are dark shaded. (b) Lag (months) between W_E and h_{OGCM} at which the maximum correlations in (a) are achieved. Positive lags indicate that W_E leads the changes in pycnocline depth.

mized. The correlation is highest in a band that extends westward from the center of the Alaskan gyre (~50°N, 145°W) to the Aleutian Islands, with values of ~0.7 (Fig. 5a). The correlations decrease toward the Alaska Peninsula where they drop to values very close to zero. Along the coastal band to the east of Kodiak Island, correlations tend to be higher (0.3–0.5) than on the western side, with maximum values of ~0.5 between Seward and Queen Charlotte Island. Figure 5b shows the lags between Ekman pumping and pycnocline depth that yield the maximum correlations. Ekman pumping variations always lead pycnocline depth variations with lags ranging from 6–8 months over a large area in the central part of the Gulf of Alaska to values as large as 10–15 months in the northern portion of the Gulf of Alaska and close to the southeastern corner of the domain. Lags are much smaller from the southern part of the Alaska Peninsula to the Aleutian Islands where Ekman pumping and pycnocline depth are only weakly correlated.

To further examine the influence of the local Ekman pumping upon pycnocline variability and understand the phase relationships between the two fields, we consider the simple model used by Lagerloef (1995) and CL02:

$$\frac{dh}{dt} = -W_E - \lambda h, \tag{2}$$

where h is the pycnocline depth, W_E is the Ekman pumping, and λ is a linear damping coefficient with the units of the inverse of time. Equation (2) is forced with monthly anomalies of Ekman pumping computed from the NCEP–NCAR reanalyses wind stress, the same forcing which drives the OGCM. Equation (2) is solved using a second-order accurate trapezoidal scheme as

$$h^{n+1} = \alpha_1 h^n + \alpha_2 W_E^{n+1/2}, \tag{3}$$

where $\alpha_1 = (2 - \lambda\Delta t)/(2 + \lambda\Delta t)$ and $\alpha_2 = (2\Delta t)/(2 + \lambda\Delta t)$. We have used the OGCM pycnocline depth anomalies at the initial time (January 1958) as initial conditions for the simple model.

A question remains concerning the value of the damping time scale λ^{-1}. CL02 found that the time evolution of the pycnocline depth produced by the simple model (h) is largely controlled by the damping time scale λ^{-1}. Longer damping time scales tend to emphasize the oceanic response at lower frequencies, and to increase the lag between Ekman pumping and pycnocline depth variations. As shown by (3), α_1 can be interpreted as the lag-1 autocorrelation of pycnocline depth. Using the lag-1 autocorrelation of yearly pycnocline depth anomalies at OWS P, CL02 found a value of 1.4 yr for λ^{-1}, while the lag-1 autocorrelation of the Pacific decadal oscillation (PDO) index [the leading principal component of monthly SST anomalies over the North Pacific, as computed by Mantua et al. (1997)] yielded $\lambda^{-1} = 1.6$ yr

CL02 used a single reference value of $\lambda^{-1} = 1.5$ yr for their entire North Pacific domain. However, if the damping term $-\lambda h$ in (2) is a parameterization of oceanic processes, the damping time scale may be expected to vary spatially depending on the strength of those processes. Using the OGCM as a term of comparison, we have determined the value of λ^{-1} that maximizes the instantaneous correlation with the OGCM time series at each grid point. The resulting distribution (Fig. 6a) shows indeed large spatial variability of the damping time scale, ranging from 14–16 months in the central part of the Gulf of Alaska to values as large as 90 months along the coastal band to the east of Kodiak Island. In the area along the Alaska Peninsula from Kodiak Island to the Aleutian Islands λ^{-1} is close to 12

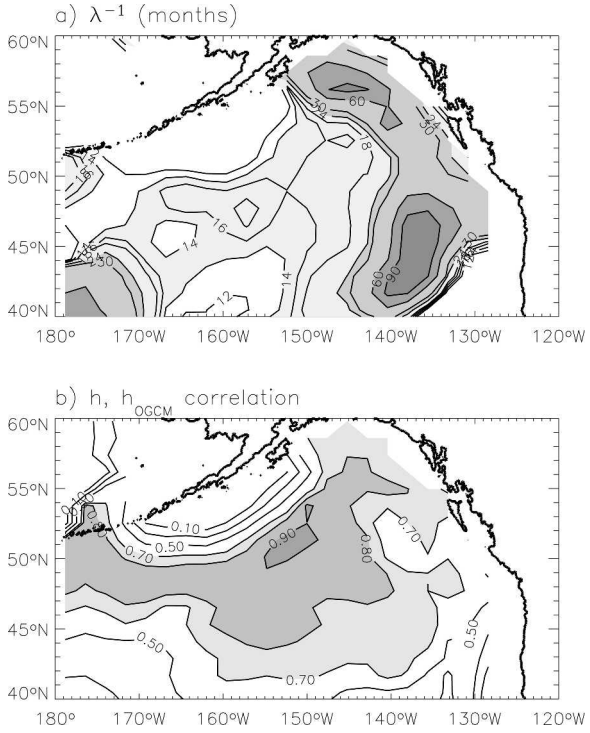

FIG. 6. (a) Spatial distribution of the damping time scales λ^{-1} (months), which maximizes the correlation between pycnocline depth anomalies produced by the Ekman pumping model (2) and the pycnocline depth anomalies in the OGCM. (b) Spatial distribution of the correlation between h and h_{OGCM} obtained using the values of λ in (a). Light shading is for values larger than 0.7, intermediate shading is for values larger than 0.8, and dark shading is for values larger than 0.9.

months, but correlations are very low in this area (Fig. 6b). The values we find for the damping time scale in the central part of the Gulf of Alaska (14–18 months) are in agreement with Lagerloef (1995) and CL02's estimates.

The pattern of λ^{-1} in Fig. 6a is generally consistent with the spatial distribution of the lags between W_E and pycnocline depth in Fig. 5a. However, it may be seen from (2) that the phase lag between h and W_E is frequency dependent and given by $\Phi = \mathrm{atan}\,(\omega\lambda^{-1})$, where ω is the angular frequency. Thus, Φ depends upon the ratio between the frictional time scale λ^{-1} and the period of the forcing $2\pi\omega^{-1}$, varying from values very close to 0° when the period of the forcing is much longer than the frictional time scale to $\pi/2$ for forcing periods much shorter than the frictional time scale. Thus, at low frequencies Ekman pumping and pycnocline depth variations tend to be in phase, while at high frequencies they are in quadrature. Comparison between Figs. 5b and 6a shows that the lag between Ekman pumping and pycnocline depth response is generally larger in areas where λ^{-1} is larger. In the central part of the Gulf of Alaska λ^{-1} ~15 months. Considering a period of 3 yr for the forcing (recall that the Ekman pumping used for the correlations only contains periods longer than 2 yr) the time lag is ~7 months, very close to the lag between W_E and OGCM pycnocline depth in the same area (Fig. 5b).

The pattern of correlations between h and h_{OGCM} obtained with the values of λ^{-1} in Fig. 6a is shown in Fig. 6b. The overall structure is similar to the correlation pattern between W_E and h_{OGCM}, but the correlations between h and h_{OGCM} are higher than the correlations between W_E and h_{OGCM} because of a larger level of high-frequency variability in the W_E field with respect to the h field. The correlations in Fig. 6b indicate that the simple model gives an excellent fit to the OGCM in the central part of the Gulf of Alaska, and west of ~145°W, with maximum correlations (0.9) at approximately 50°–52°N, 155°–150°W. Correlations decrease onshore, especially toward the Alaska Peninsula and to the south of ~45°N. To the east of Kodiak Island values range from 0.5 south of Queen Charlotte Island to 0.7 between Queen Charlotte Island and Kodiak Island, while southwestward of Kodiak Island correlations drop to near zero. Thus, the area to the southwest of Kodiak Island is the region where the simple model completely fails to reproduce the OGCM pycnocline depth changes. This is the region of the Alaskan Stream, a strong western boundary current. Advection processes can be expected to be important in this area and be responsible for the inability of the simple model to reproduce the OGCM pycnocline variability. Satellite observations have also shown the presence of pronounced anticyclonic meanders that develop along the stream as a result of the stream instabilities (Crawford et al. 2000). These meanders, which are not captured by the OGCM because of its coarse horizontal resolution, will certainly produce large, low-frequency variability in the local pycnocline that cannot be reproduced by the simple Ekman pumping model.

To further examine the simple model fit to the OGCM, we compute the difference between pycnocline variability in the OGCM and pycnocline variability produced by Eq. (2) using the spatially varying λ^{-1} that maximizes the correlation. The standard deviation of this residual field, which is a measure of the misfit of the simple model to the OGCM, maximizes in the western part of the Gulf of Alaska (Fig. 7b) where the variance of h_{OGCM} is also very large (Fig. 7a). In particular, to the southwest of Kodiak Island the residual field accounts for 80%–90% of the variance of h_{OGCM} (Fig. 7c). The minimum of the residual standard deviation is found in the central part of the Gulf of Alaska (cen-

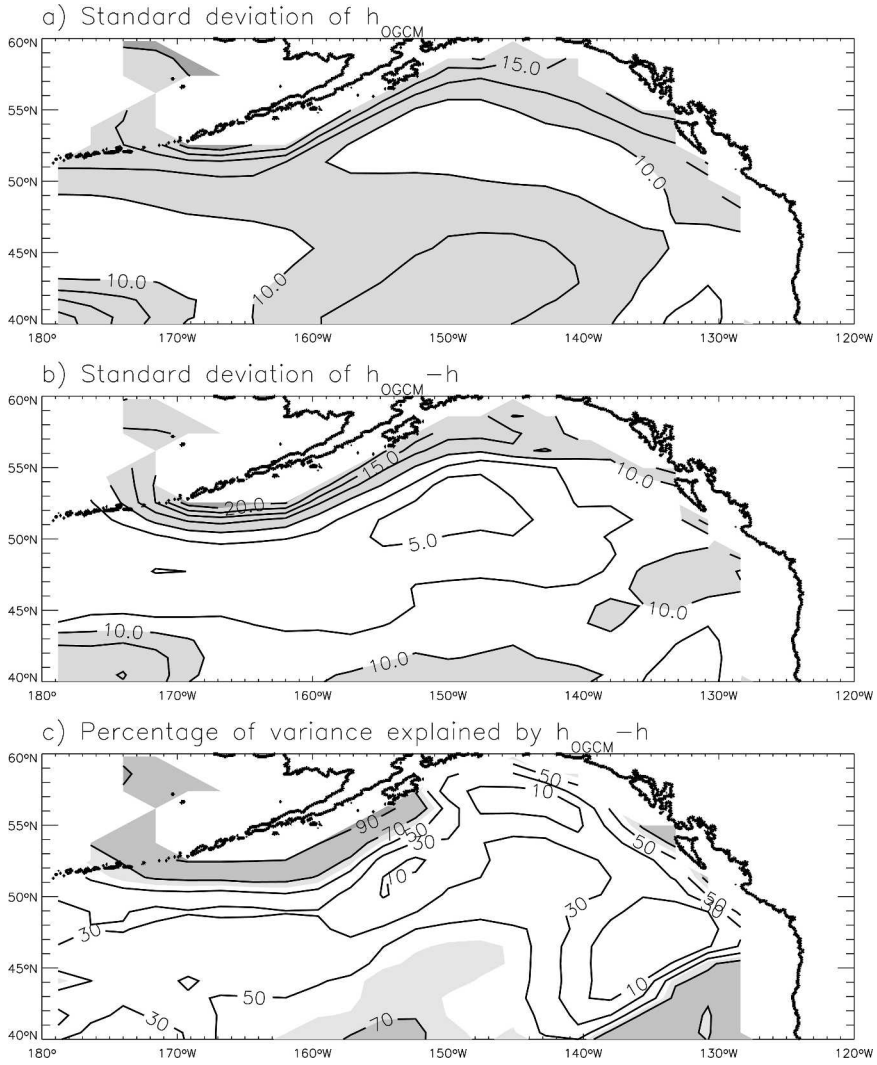

FIG. 7. (a) Standard deviation of pycnocline depth in the OGCM. Contour interval is 5 m. Values larger than 10 m are shaded. (b) Standard deviation of the residual field computed as the difference between pycnocline depth anomalies in the OGCM and pycnocline depth anomalies from the Ekman pumping model (2). Contour interval is 5 m. Values larger than 10 m are shaded. (c) Percentage of the OGCM pycnocline depth variance accounted for by the residual field. Values larger than 60% are light shaded, and values larger than 70% are dark shaded.

tered around 52°N, 150°W), where (2) produces the best fit to the OGCM. In this area the variance of the residual field accounts for 10%–30% of the OGCM pycnocline depth variance (Fig. 7c).

5. Rossby wave dynamics

Equation (2) emphasizes the importance of local Ekman pumping in driving thermocline variability. Satellite altimetry, on the other hand, has provided evidence of westward propagating SSH anomalies, which appear to be associated with first-mode baroclinic Rossby waves (Kelly et al. 1993; Qiu 2002; Fu and Qiu 2002). What fraction of pycnocline variability in the OGCM is due to Rossby wave propagation? To answer this question we compare the performance of the local Ekman pumping model (2) with that of a Rossby wave model. A direct comparison is carried out along two latitudes, 40.5° and 49°N. As seen in Fig. 6b, the local Ekman pumping model gives a good fit to the OGCM along 49°N with correlations of ~0.8 west of 140°W, but its performance is worse along 40.5°N where the maximum correlations are less than 0.7.

Following CL04, we consider a linear, reduced-

gravity, quasigeostrophic model to simulate upper-ocean variability that includes Rossby wave dynamics. The wavelength of Rossby waves at interannual time scales is typically longer than ~2000 km (Chelton and Schlax 1996; Fu and Chelton 2001), while the Rossby radius of deformation is ~30 km around 40°N (Chelton et al. 1998) and decreases poleward. Thus, the long-wave approximation is valid poleward of 40°N. In the long-wave limit the equation describing the evolution of pycnocline depth is

$$\frac{\partial h_R}{\partial t} + c_R \frac{\partial h_R}{\partial x} = -W_E - \lambda_1 h_R, \tag{4}$$

where h_R is the pycnocline depth anomaly in the presence of Rossby wave propagation, $c_R = -\beta R^2$ is the phase speed of long baroclinic Rossby waves, where R is the Rossby radius of deformation and β is the latitudinal gradient of the Coriolis parameter, and λ_1 is a Rayleigh friction coefficient. Following Killworth et al. (1997), who took into account the influence of a background mean flow, we have chosen $c_R = 0.8$ cm s^{-1} along 49°N and 1.5 cm s^{-1} along 40.5°N. To optimize the comparison with the OGCM λ_1 has been chosen to be (4 yr)$^{-1}$. Equation (4) can be solved by integrating along Rossby wave characteristics in the x–t plane:

$$h_R(x, t) = h_R(x_E, t - t_E)e^{-\lambda_1 t_E} + \int_{x_E}^{x} \frac{W_E(\xi, t - t_\xi)}{c_R(\xi)} e^{-\lambda_1 t_\xi} d\xi, \tag{5}$$

where the solution at each point x and time t is obtained as the superposition of the disturbances generated east of point x at previous times. The first term on the rhs of (5) is the contribution of the signals originating at the eastern boundary x_E, and reaching point x at time t with a transit time $t_E = \int_{x_E}^{x} [d\xi/c_R(\xi)]$. The second term on the rhs of (5) is the contribution of the disturbances generated by the Ekman pumping east of the target point x with $t_\xi = \int_{\xi}^{x} [ds/c_R(s)]$. Both boundary and wind-forced terms decay while propagating counterclockwise with the frictional time scale $1/\lambda_1$.

Figures 8 and 9 show the comparisons between the evolution of pycnocline depth anomalies from the OGCM and those obtained from the Ekman pumping model (2) and Rossby wave model (4) along 49° and 40.5°N, respectively. The pycnocline depth variations in the OGCM along 49°N (Fig. 8a) exhibit a clear change in character after 1976 with positive anomalies west of ~145°W before the shift and negative afterward. Pycnocline depth anomalies east of 145°W tend to be of opposite sign to those farther west, consistent with Fig. 1. Westward propagation is evident at times: for example the positive anomaly centered at ~155°W in 1965 and the negative anomaly centered around the same longitude in 1987. However, in most cases pycnocline depth anomalies exhibit a standing character. The evolution produced by the Ekman pumping model (Fig. 8b) does not capture the westward propagation seen in the OGCM but reproduces relatively well other aspects of the variability. The Rossby wave model, on the other hand, gives a good representation of the westward-propagating anomalies but does not capture other features, for example the anomalies west of 170°W during 1958–66 and 1975–87 (Fig. 8c). It is worth noting that the period examined by Fu and Qiu in the altimeter data (1993–2000) contains a prominent westward-propagating signal. To quantify the goodness of the fit of the Ekman pumping and Rossby wave models to the OGCM we show in Fig. 10a the instantaneous correlations of each model with the OGCM along 49°N. Overall, the Ekman pumping model produces a better fit to the OGCM than the Rossby wave model, indicating that over the 1958–97 period Rossby wave propagation is not the controlling dynamics along 49°N.

Along 40.5°N, the evolution of the pycnocline depth anomalies in the OGCM does not show any clear indication of the 1976–77 climate shift. Westward propagation, as indicated by the slope of the phase lines, can be noticed for some events east of ~165°W. However, the large-scale anomalies appear to be primarily of standing nature, an aspect captured relatively well by the Ekman pumping model. Along this latitude the performance of the two simple models is comparable, as indicated by the instantaneous correlation with the OGCM (Fig. 10b).

6. Sverdrup dynamics

A classical model of the mean circulation of the Gulf of Alaska would include a Sverdrup interior with the Alaskan Stream as the western boundary current. Are the changes in the Alaskan Stream that took place after the mid-1970s consistent with Sverdrup dynamics? If the Alaskan Stream does respond to the adjustment of the Alaska gyre according to Sverdrup dynamics, this could partially explain why its variability is only weakly affected by the local wind stress curl.

Sverdrup balance (Sverdrup 1947) is derived from the vertical integral of the vorticity equation

$$\beta v = f \frac{\partial w}{\partial z}, \tag{6}$$

where v is the meridional velocity, w is the vertical velocity, and z is the vertical coordinate. Equation (6)

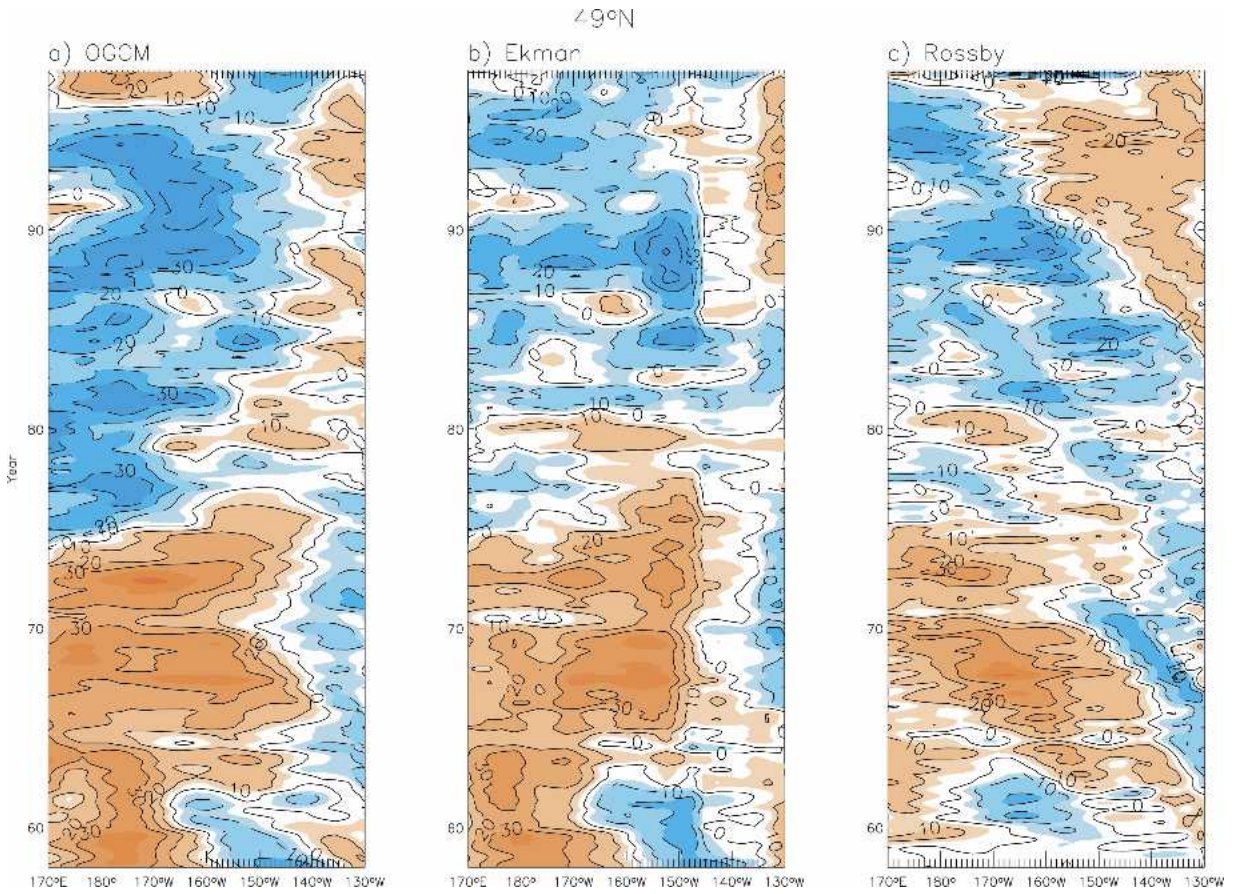

FIG. 8. Comparison between the evolution of pycnocline depth along 49°N in (a) the OGCM, (b) the one computed from the Ekman pumping model, and (c) the one obtained from the Rossby wave model. The solution for the Ekman pumping model was obtained by using the optimal values of λ in Fig. 6a along 49°N. Dashed contours and blue shading are for negative pycnocline depth anomalies (shallower pycnocline), while solid contours and orange shading are for positive anomalies (deeper pycnocline). Contour interval is 10 m in all three panels.

states that the potential vorticity changes associated with the vertical stretching of the water column must be balanced by the changes in planetary vorticity due to meridional motions. Integrating (6) from a level of no-motion to the base of the Ekman layer, we obtain the classical form of the Sverdrup balance:

$$\beta V_g = f W_E, \tag{7}$$

where V_g is the vertically integrated geostrophic meridional velocity. The condition of nondivergence for the vertically integrated geostrophic flow allows to introduce a streamfunction ψ_g, such that

$$V_g = \frac{\partial \psi_g}{\partial x}. \tag{8}$$

Using the boundary condition that $\psi_g(x_E) = 0$ at the eastern boundary x_E of the ocean basin, the geostrophic streamfunction at longitude x along a given latitude can be computed by integrating westward from the eastern boundary:

$$\psi_g(x) = -\frac{f}{\beta}\int_{x_E}^{x} W_E\, dx'. \tag{9}$$

The time averaged barotropic streamfunction in the model describes the cyclonic circulation of the Alaska gyre (Fig. 11a). The mean transport of the model Alaskan Stream is ~7–8 Sv (Sv ≡ 10^6 $m^3\,s^{-1}$), a value smaller than some observational estimates. Geostrophic transports relative to 1500 dbar are typically 12–18 Sv (Musgrave et al. 1992). However, intermittent surveys of the Alaskan Stream yielded a broad range of transport estimates with values as low as 2 Sv and as large as 20 Sv (Reed et al. 1980; Royer 1981). The barotropic streamfunction difference between 1977–97 versus 1960–75 (Fig. 11b) shows a slight weakening of the circulation in the eastern part of the basin and a

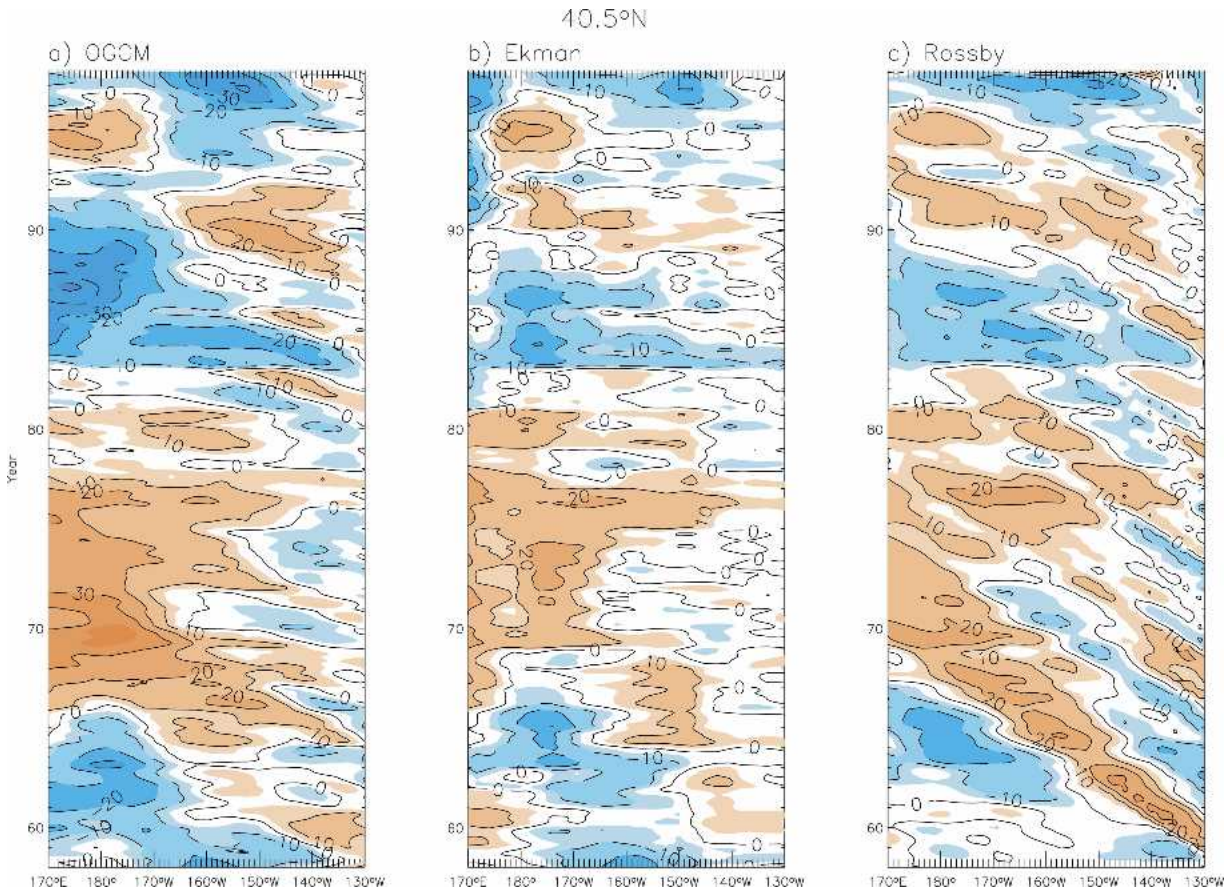

FIG. 9. As in Fig. 8 but for 40.5°N.

strengthening of the circulation to the southwest of Kodiak Island. The intensification of the Alaskan Stream after the mid-1970s is consistent, by geostrophy, with the more pronounced doming of the isopycnals after the mid-1970s (Fig. 2), and resulting larger zonal density gradients (Fig. 1).

The changes in barotropic streamfunction associated with the 1976–77 climate shift, as predicted by (9), have been computed using the Ekman pumping difference (period 2 − period 1) based on annual values. The annual Ekman pumping changes have a spatial structure that is very similar to the winter difference (Fig. 5), but the magnitude of the changes is generally smaller. The result (Fig. 11c) shows significant differences with the streamfunction changes found in the OGCM. The circulation changes implied by the Sverdrup balance include an intensification of the Alaskan Stream only south of 54°N, while north of this latitude the flow weakens appreciably, with transport changes as large as 2 Sv. Thus, the Sverdrup balance does not seem to provide a good description of the wind-forced circulation changes in the Gulf of Alaska after the mid-1970s.

7. Coastal propagation of pycnocline depth anomalies

We have seen in section 4 that the agreement between the Ekman pumping model (2) and the OGCM deteriorates in a broad band along the coast, particularly in the western side of the Gulf of Alaska. This band is characterized by the cyclonic circulation of the subpolar gyre, as shown in Fig. 12, where the OGCM average velocities above the pycnocline (identified by the 26.4 σ_θ isopycnal) are displayed. The primary currents include a broad northward flowing eastern boundary current, the Alaska Current, which becomes narrower and stronger in the apex of the gyre and continues southwestward along the Alaska Peninsula as the Alaskan Stream. Thus, it is conceivable that advection processes may influence the evolution of pycnocline depth anomalies in this area. The OGCM is too coarse to resolve mesoscale variability, but in the real world the presence of long-lived eddies and meanders (Crawford et al. 2000) can also produce low-frequency pycnocline variability that is not captured by the simple

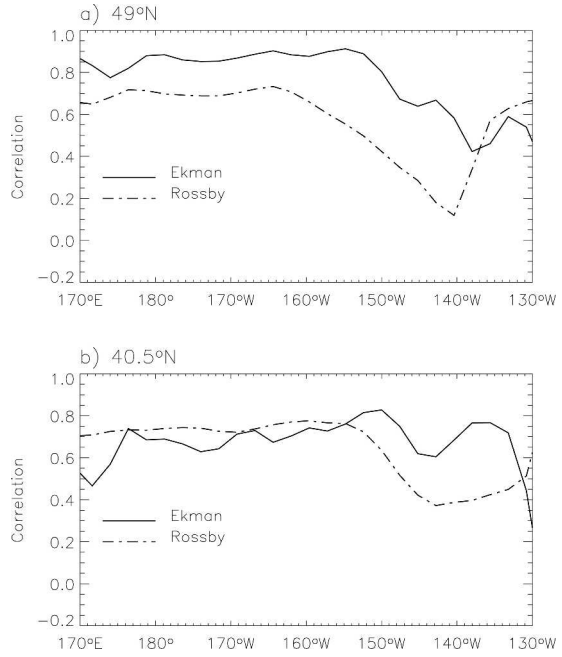

FIG. 10. (a) Instantaneous correlations between the pycnocline depth anomalies in the OGCM and those computed with the local Ekman pumping model (solid line), and the Rossby wave model (dot–dash line) along 49°N. (b) As in (a) but along 40.5°N.

Ekman pumping model. To examine propagation phenomena along the coastal band we consider a curved path that approximately follows the coast and lies along the axis of the Alaska Current and Alaskan Stream, as shown in Fig. 13a. Some points along the path (A, B, C, D, and E) have been highlighted as reference points. Figure 13b shows the time evolution of h_{OGCM} at points A, B, and C, smoothed using a three-point binomial filter. The OGCM pycnocline variations at point A lag the pycnocline variations at point B by 4 months, with a maximum correlation coefficient of 0.96, and lag the variations at point C by ~6 months, with a maximum correlation coefficient of 0.92. Thus, pycnocline variations along the path are strongly correlated at lags that increase westward, suggesting a counterclockwise propagation of the depth anomalies.

The lag correlations between pycnocline depth variations at point A and at all the points along the path (Fig. 14) show that the pycnocline depth anomalies are correlated over a very large distance along the coast and propagate counterclockwise along the path with speeds varying from approximately 16 cm s^{-1} at distances greater than 2100 km (approximately east of point C) to ~8 cm s^{-1} between 600 and 2100 km, and decreasing to ~1.3 cm s^{-1} at the western end of the path, as indicated by the slope of the dot–dash line in Fig. 14. The dot–dash line shows the approximate inclination of the phase lines and has been computed by fitting a straight line through the points of maximum correlations. Using different points along the path as reference points for the lag correlations leads to different estimates of propagation speeds, especially in the eastern part of the path, approximately east of point C where propagation appears to be faster when reference points east of point A are considered. In all cases, propagation speeds appear to increase from west to east independently of the reference point chosen.

To account for the propagation of pycnocline depth anomalies, (2) has been modified to include a propagation term in the form

$$\frac{\partial h_p}{\partial t} + \upsilon \frac{\partial h_p}{\partial \zeta} = -W_E - Rh_p, \tag{10}$$

where h_p indicates the isopycnal depth displacement obtained when propagation is included, υ is the propagation velocity, ζ is the coordinate along the propagation path, and R is a Rayleigh friction coefficient. We found that the correlations and regressions between h_p and h_{OGCM} increase with decreasing values of R. So we have chosen $R = 1/100\ \mathrm{yr}^{-1}$. Equation (10) is solved by integrating along the path in Fig. 13a:

$$h_p(\zeta, t) = h_p(\zeta_s, t - t_s)e^{-Rt_s} + \int_{\zeta_s}^{\zeta} \frac{W_E(\xi, t - t_\xi)}{\upsilon(\xi)} e^{-Rt_\xi}\, d\xi. \tag{11}$$

The form of the solution is similar to the one obtained for the Rossby wave equation in (4), but in this case the solution at each point ζ and time t is obtained as the superposition of the disturbances generated upstream of point ζ at previous times. The first term on the rhs of (5), h_{PS}, is the contribution of the signals present at the starting point of the path ζ_s, and reaching point ζ at time t with a transit time $t_s = \int_{\zeta_s}^{\zeta} [d\xi/\upsilon(\xi)]$. The second term on the rhs of (5), h_{PE}, is the contribution of the disturbances generated by the Ekman pumping east of the target point ζ, with $t_\xi = \int_{\xi}^{\zeta} [ds/\upsilon(s)]$.

Using the estimates of propagation speed from the lag-correlations in Fig. 14 as a guideline, we have chosen $\upsilon(\zeta)$ to increase from 3 cm s^{-1} at the western end of the path to 7.5 cm s^{-1} approximately between points A and C, 10 cm s^{-1} around point C, and reaching a maximum value of 22 cm s^{-1} upstream of point C. The fit of Eq. (10) to the OGCM does not seem to be very sensitive to the values of propagation speed used. Monthly anomalies of pycnocline depth at point E (see Fig. 13a) in the OGCM have been used as boundary condition $h_p(\zeta_s, t)$ in (11).

The resulting correlations between h_p and h_{OGCM} along the coastal path are shown in Fig. 15a, where they are compared with the correlations between h_{OGCM} and

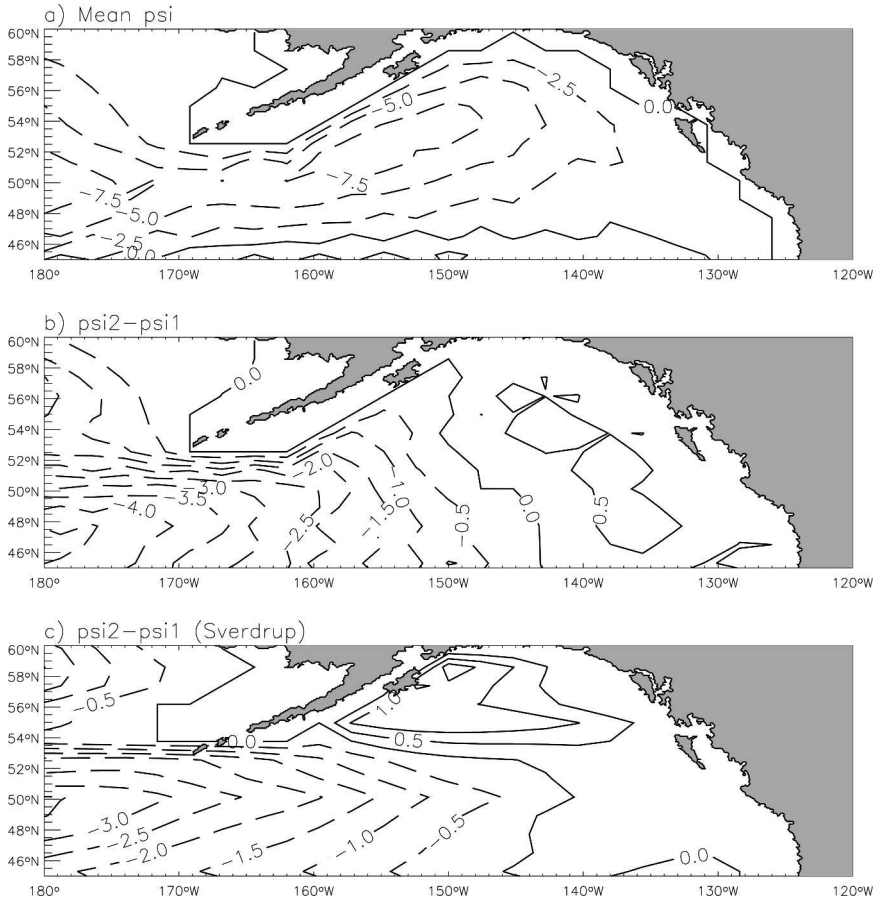

FIG. 11. (a) Mean model barotropic streamfunction over the Gulf of Alaska, describing the cyclonic circulation of the model Alaska Gyre. (b) Difference of barotropic streamfunction between 1977–97 and 1960–75. (c) Difference in barotropic streamfunction implied by Sverdrup dynamics, computed as the zonal integral of the annual Ekman pumping difference. Contour intervals are 2.5 Sv in (a) and 0.5 Sv in (b) and (c). Solid contours are for positive values, and dashed contours are for negative values.

the pycnocline displacements h obtained with the local Ekman pumping model without propagation. The correlations between h and h_{OGCM} maximize (~0.7) just to the west of point C along the path, but they drop to values close to zero south of point D (4000–5000 km from the western end of the path), and southwest of point B (Kodiak Island). On the contrary, when propagation is included, correlations are ~0.7–0.8 over most of the path, and increase to larger values when approaching the boundary point E. Thus, over most of the path, propagation appears to have a large influence on pycnocline depth evolution. In particular, the pycnocline depth variations to the southwest of Kodiak Island (500–1500 km from the western end) result entirely from the propagation into that area of pycnocline depth anomalies originating further upstream, since the local Ekman pumping would tend to produce anomalies of the opposite sign.

How much of the pycnocline variability along the coastal path is due to the downstream propagation of the displacements at point E (h_{ps}), and what fraction is forced by the Ekman pumping along the path? The

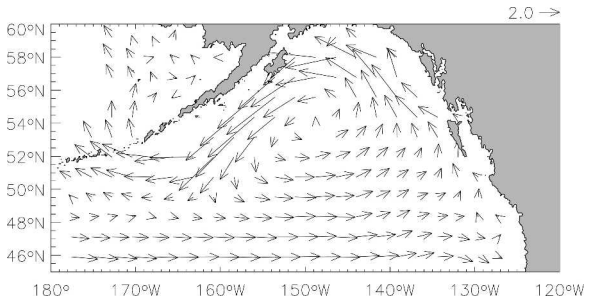

FIG. 12. Average upper-layer velocities (cm s^{-1}) in the OGCM. The upper layer is defined as the layer extending from the surface to the depth of the 26.4 σ_θ isopycnal, which is used as proxy for pycnocline depth.

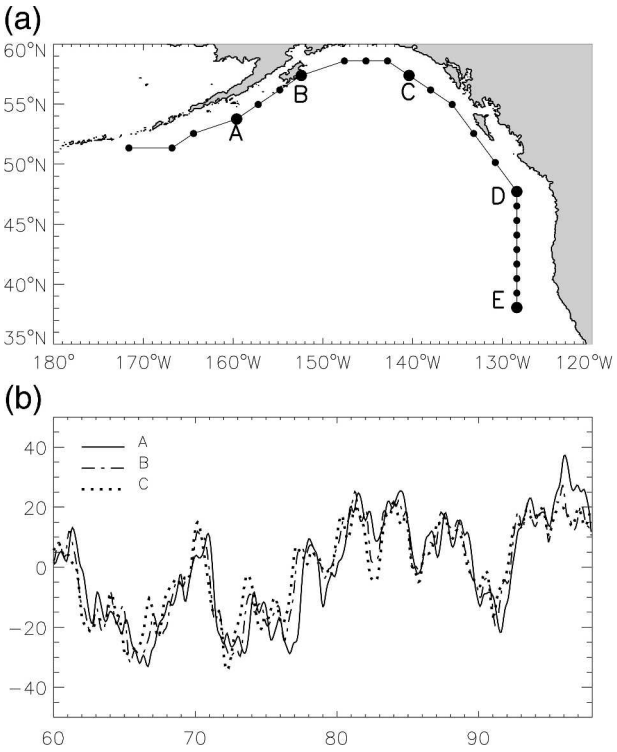

FIG. 13. (a) Coastal path along which lag correlations of pycnocline depth anomalies in the OGCM are considered. The points A, B, C, D, and E are highlighted for reference. (b) Time series of h_{OGCM} at point A (solid line), B (dot–dash line), and C (dotted line). The time series have been smoothed with a three-point binomial filter. The pycnocline variability at point A lags the pycnocline variability at point B by ~4 months (correlation coefficient = 0.96), and the pycnocline variability at point C by ~6 months (correlation coefficient = 0.92).

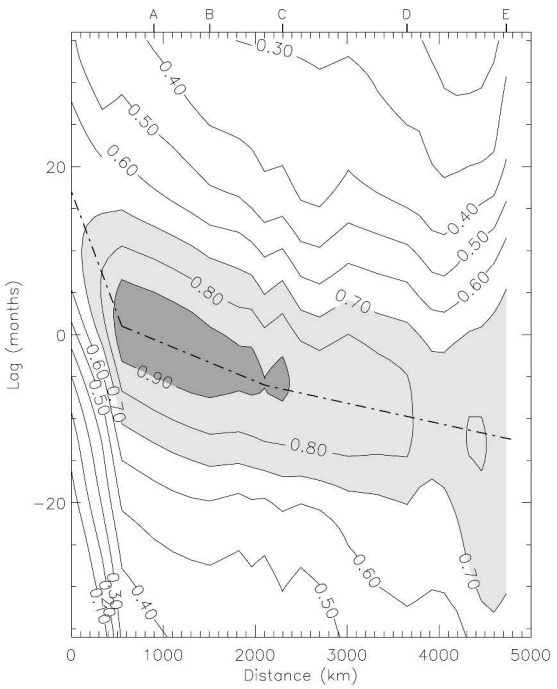

FIG. 14. Lag correlations between pycnocline depth variations at point A in Fig. 13a and all the points along the coastal path. Values larger than 0.7 are light shaded, and values larger than 0.9 are dark shaded. The dot–dashed line indicates the approximate slope of the phase lines in three different areas along the path, corresponding to propagation speeds of ~1.3, 8.6, and 16 cm s^{-1} from west to east. The lags yielding the maximum correlation at each distance have been used as a guideline to draw the dot–dash lines. Distance is computed starting at the westernmost point. To associate the distance with specific locations along the path, the points A, B, C, D, and E in Fig. 13a are indicated along the top axis.

structure of the solution [Eq. (11)] allows to separate the two contributions. Shown by the dotted line in Fig. 15a is the correlation between h_{ps} and h_{OGCM} along the path, indicating that the downstream propagation of the signals at point E can account for most of the correlations along the path. However, the lower correlations of h_{ps} and h_{OGCM} relative to h_p and h_{OGCM} downstream of ~3000 km from the western end of the path suggest that the Ekman pumping between the distances of 1800 and 3000 km may influence the variability. In this area the local Ekman pumping model also yields correlations comparable to those obtained including propagation. The area between 1800 and 3000 km from the western end of the path is where the largest negative Ekman pumping changes associated with the 1976–77 climate shift are found (Fig. 5).

Although the inclusion of propagation considerably improves the performance of the simple model, there are still some discrepancies with the OGCM, especially in the amplitude distributions along the path, as shown by the regression of h_{p} upon h_{OGCM} (Fig. 15b, solid line): regressions decrease from unity at point E, where the pycnocline depth anomalies coincide with the OGCM values, to ~0.5 at the western end of the path, indicating that the simple model (10) tends to underestimate the amplitude of the pycnocline displacements in the OGCM. When only h_{ps} is considered (dotted line in Fig. 15b), the amplitude of the OGCM pycnocline variability is further underestimated downstream of point C. The regression between h and h_{OGCM} is also shown for comparison in Fig. 15b (dot–dash line): apart from the area between points B and C where the regressions between h and h_{OGCM} are comparable to those between h_p and h_{OGCM} the local Ekman pumping model greatly underestimates the amplitude of the OGCM pycnocline variability, in particular upstream of point D and downstream of point B, indicating that in those areas propagation is essential. Thus, the correlation and regression analyses suggest that the Ekman pumping forcing can play a role in exciting pycnocline variability in the area

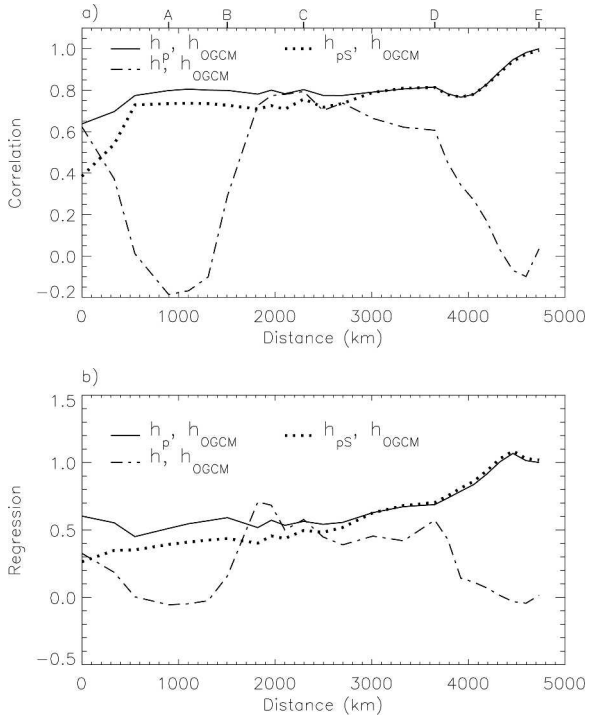

FIG. 15. (a) The solid line shows the correlation between isopycnal depth displacements obtained from the Ekman pumping model with propagation (h_p) and the isopycnal depth displacements in the OGCM (h_{OGCM}) along the coastal path in Fig. 13a. The dot–dashed line shows the correlation between the isopycnal depth variations from the Ekman pumping model without propagation (h) and h_{OGCM} along the path. (b) Same as (a) but regressions are displayed instead of correlations.

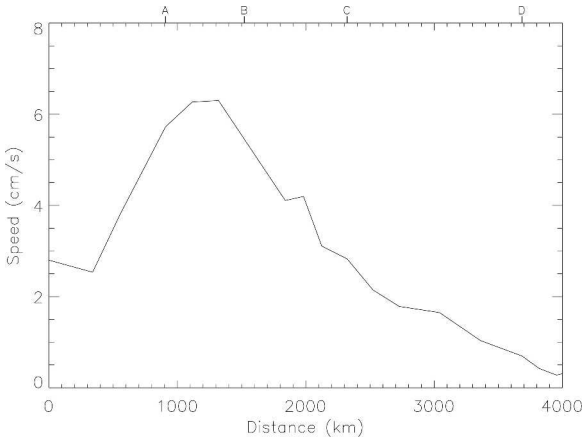

FIG. 16. Winter (Dec–Apr) upper-ocean speed as a function of distance along the coastal path in Fig. 13a in the OGCM. The upper-ocean speed has been estimated by vertically integrating the model speed from the surface to the depth of the 24.6 σ_θ isopycnal, assumed as proxy for pycnocline depth. The points A, B, C, and D shown in Fig. 13a are indicated along the top axis for orientation purposes.

around point C, and the wind forced anomalies are then advected downstream.

Are the propagation speeds inferred from the lag correlations consistent with mean flow advection? The velocities in the OGCM vary strongly with depth, and we need to first determine what is the advective velocity of pycnocline depth. As a conceptual framework we consider a two-layer quasigeostrophic model with layer thicknesses H_1 and H_2 and mean velocities U_1 and U_2 for the first and second layers, respectively (Pedlosky 1996). For this system the advective velocity U_A is

$$U_A = \frac{U_2H_1 + U_1H_2}{H_1 + H_2}. \tag{12}$$

Thus, if the two layers have equal depths ($H_1 = H_2$), the advective velocity is simply the average velocity $0.5(U_1 + U_2)$. If, on the other hand, $H_1 \ll H_2$, then $U_A \sim U_1$. In winter the Gulf of Alaska can be viewed as a two-layer system, where the two layers are separated by the halocline. The upper-layer thickness is ~100–150 m, and it is reasonable to assume that $H_1 \ll H_2$. Thus, the advective velocity in the model can be estimated by vertically averaging the model velocity from the surface to the depth of the pycnocline. Figure 16 shows the model speed, averaged from the surface to the depth of the 26.4 σ_θ isopycnal, which we have used as proxy for pycnocline depth, along the coastal path in Fig. 13a. The upper-layer speed increases from 0.5 cm s^{-1} at point D to a maximum value of ~6.5 cm s^{-1} between point A and Point B (the model's Alaskan Stream) and then decreases again to ~3 cm s^{-1} at the western end of the path. While the upper-layer speeds are comparable with the propagation speeds estimated from the lag-correlation analysis to the west of point B, they are much smaller than the propagation speed to the east of point B. Thus, propagation through mean flow advection seems possible to the southwest of Kodiak Island (point B), but farther east the model mean velocity is too small to explain the depth anomaly propagation. Boundary waves, as described in several observational studies (e.g., Enfield and Allen 1980; Chelton and Davis 1982; Qiu 2002) may be responsible for the propagation of pycnocline depth anomalies in the eastern part of the basin.

8. Summary and discussion

In this paper we have examined the influence of local Ekman pumping and horizontal propagation processes upon pycnocline depth variability in the Gulf of Alaska, using the output from an ocean general circulation model forced with observed surface fields over the pe-

riod 1958–97. The evolution of the OGCM pycnocline depth has been compared with observations at two locations in the Gulf of Alaska, where long-term measurements of the upper-ocean density structure are available (Ocean Weather Station P at 50°N, 145°W, and Station GAK1 at 59°N, 149°W). The winter pycnocline depth changes in the OGCM agree relatively well with those observed at both interannual and longer time scales, especially during periods with more measurements. The low-frequency evolution of the pycnocline depth is dominated by the 1976–77 climate regime shift. After the mid-1970s, the model shows a deepening of the pycnocline in a broad band following the coast and shoaling of the pycnocline in the central part of the Gulf of Alaska. These changes are consistent with the low-frequency evolution of the pycnocline depth at Station GAK1, where the pycnocline exhibits a deepening trend, and at OWS P, where a shoaling trend is observed.

To understand what fraction of the OGCM pycnocline depth variability can be driven by local Ekman pumping, we have introduced a simple model for the evolution of pycnocline depth, where the forcing is supplied by the local Ekman pumping and dissipative processes are modeled with a linear damping term. This model is very similar to the one used by Lagerloef (1995) and CL02. Solutions to the Ekman pumping model have been computed for different values of the damping time scale. Correlations between pycnocline depth variations from the simple model and from the OGCM maximize toward the center of the Alaska gyre, where the solution of the simple model accounts for a large fraction of the OGCM pycnocline depth variability. Correlations decrease along a broad coastal band and, in particular, to the southwest of Kodiak Island where they drop to values very close to zero. In this area the pycnocline deepens, while the Ekman pumping changes are indicative of enhanced upwelling. The damping time scales that yield the maximum correlations between the OGCM and the simple model are characterized by a spatial pattern with values ranging from 14–18 months in the central part of the Gulf of Alaska to values as large as 90 months at some locations along the coast. The damping time scales in the central part of the Gulf of Alaska, where correlations are higher, are very similar to those estimated by Lagerloef (1995) and CL02 using statistical methods.

Westward-propagating Rossby waves can be detected in the evolution of the model pycnocline. Propagating features cannot be reproduced by the local Ekman pumping model, but can be modeled with the explicit inclusion of a zonal propagation term. However, large-scale pycnocline depth anomalies in the OGCM have a predominantly standing character that is well captured by the Ekman pumping model. This result is in agreement with the study of Cummins and Lagerloef (2004) based on the comparison of the local Ekman pumping model and a quasigeostrophic model with satellite data over the period 1993–2003.

Pycnocline depth anomalies exhibits a counterclockwise propagation along the coastal band, clearly indicating that Ekman pumping alone cannot account for the pycnocline variability in that area. This coastal propagation may be due to either mean flow advection or boundary waves. The inclusion of propagation, with a speed estimated from the OGCM, considerably improves the agreement with the OGCM along the coastal path. The physical nature of the propagation velocity remains an open question. Along the western half of the path pycnocline depth anomalies appear to propagate with a speed that is very similar to the OGCM upper-layer mean speed, so propagation could be consistent with mean flow advection. However, the propagation speed increases eastward to values that are much larger than the upper-layer mean speed in the OGCM. Thus, in the eastern part of the path boundary waves appear to be a more likely cause of pycnocline depth anomalies propagation. Inviscid boundary waves have an offshore scale of the order of the first baroclinic Rossby radius of deformation, which in the Gulf of Alaska is only 15–20 km (Chelton et al. 1998), and one may expect a severe distortion of these waves in a model with coarse horizontal resolution. In the presence of lateral viscosity the offshore scale of the Kelvin wave increases while the alongshore phase speed decreases because of the combined effect of lateral viscosity and limited model resolution (Hsieh et al. 1983). If the model resolution is fine enough to resolve the broader offshore scale of the viscous wave, then the alongshore phase speed is essentially determined by viscosity, but if the model resolution is still too coarse to resolve the wave structure then the propagation speed is also dependent upon the model resolution. Given the viscosity used in the model, the offshore scale of the waves may be marginally resolved by the model, but it is unclear how realistic the model's viscosity is and how distorted boundary waves may be in this numerical simulation. On the other hand, the agreement of the OGCM pycnocline variations with the pycnocline variations observed at Station GAK1 suggests that propagation speeds in the model may not be too unrealistic. Further studies are needed to clarify the nature of the propagating signals in the OGCM and the degree of distortion of these signals introduced by the model's viscosity and resolution.

The large changes in upper-ocean density structure

and circulation that took place after the mid-1970s do not seem to result from the dynamical adjustment of the Alaska gyre according to Sverdrup theory. The latter would imply a weakening of the circulation north of ~54°N, while the circulation changes in the model exhibit an intensification of the Alaskan Stream starting upstream of Kodiak Island. Sverdrup balance is achieved through Rossby wave propagation, but Rossby wave propagation can account for only a part of the pycnocline variability in the OGCM (section 5). On the other hand, propagation of pycnocline depth anomalies along the coast seems to have a significant impact on the pycnocline changes along the Alaska Peninsula, and may be responsible for some of the changes in the density structure and related circulation changes. Further studies with high-resolution models are needed to elucidate the processes responsible for the adjustment of the Alaska gyre to variations in surface wind forcing at time scales ranging from seasonal to decadal–interdecadal.

Acknowledgments. We thank the NCAR Oceanography Section for making the model output available to us. We also thank Dr. Patrick Cummins for providing the observed time series of winter pycnocline depth at Ocean Weather Station P, as well as useful comments on the manuscript, and the GLOBEC program for the long-term measurements at station GAK1. Doctor E. Firing and an anonymous reviewer have offered very valuable comments and suggestions that have greatly improved the manuscript. Author AC was supported by the NOAA/CIFAR program, and AJM was supported by NOAA/CIFAR (NA17RJ1231), NSF (OCE00-82543), and DOE (DE-FG03-01ER63255). The views expressed herein are those of the authors and do not necessarily reflect the views of NOAA or any of its subagencies.

REFERENCES

Chelton, D. B., and R. E. Davis, 1982: Monthly mean sea-level variability along the west coast of North America. *J. Phys. Oceanogr.,* **12,** 757–784.

——, and M. G. Schlax, 1996: Global observations of oceanic Rossby waves. *Science,* **272,** 234–238.

——, R. A. de Szoeke, M. G. Schlax, K. El Naggar, and N. Siwertz, 1998: Geographical variability of the first baroclinic Rossby radius of deformation. *J. Phys. Oceanogr.,* **28,** 433–460.

Crawford, W. R., J. Y. Cherniawsky, and M. G. G. Foreman, 2000: Multi-year meanders and eddies in the Alaskan Stream as observed by TOPEX/Poseidon altimeter. *Geophys. Res. Lett.,* **27,** 1025–1028.

Cummins, P. F., and G. S. E. Lagerloef, 2002: Low-frequency pycnocline depth variability at ocean weather station P in the northeast Pacific. *J. Phys. Oceanogr.,* **32,** 3207–3215.

——, and ——, 2004: Wind-driven interannual variability over the northeast Pacific Ocean. *Deep-Sea Res. I,* **51,** 2105–2121.

Deser, C., M. A. Alexander, and M. S. Timlin, 1999: Evidence for a wind-driven intensification of the Kuroshio Current Extension from the 1970s to the 1980s. *J. Climate,* **12,** 1697–1706.

Doney, S. C., S. Yeager, G. Danabasoglu, W. G. Large, and J. C. McWilliams, 2003: Modeling global oceanic interannual variability (1958–1997): Simulation design and model-data evaluation. NCAR Tech. Note NCAR/TN-452+STR.

Enfield, D. B., and J. S. Allen, 1980: On the structure and dynamics of monthly mean sea level anomalies along the Pacific coast of North and South America. *J. Phys. Oceanogr.,* **10,** 557–578.

Freeland, H. J., K. Denman, C. S. Wong, F. Whitney, and R. Jacques, 1997: Evidence of change in the winter mixed layer in the northeast Pacific Ocean. *Deep-Sea Res.,* **44,** 2117–2129.

Fu, L.-L., and D. B. Chelton, 2001: Large-scale ocean circulation and variability. *Satellite Altimetry and Earth Sciences,* L.-L. Fu and A. Cavenave, Eds., Academic Press, 133–169.

——, and B. Qiu, 2002: Low-frequency variability of the North Pacific Ocean: The roles of boundary- and wind-driven baroclinic Rossby waves. *J. Geophys. Res.,* **107,** 3220, doi:10.1029/2001JC001131.

Gargett, A. E., 1997: The optimal stability 'window': A mechanism underlying decadal fluctuations in North Pacific salmon stocks? *Fish. Oceanogr.,* **6,** 109–117.

Gent, P. R., and J. C. McWilliams, 1990: Isopycnal mixing in ocean circulation models. *J. Phys. Oceanogr.,* **20,** 150–155.

——, F. O. Bryan, G. Danabasoglu, S. C. Doney, W. R. Holland, W. G. Large, and J. C. McWilliams, 1998: The NCAR Climate System Model global ocean component. *J. Climate,* **11,** 1287–1306.

Haney, R. L., 1971: Surface thermal boundary condition for ocean circulation models. *J. Phys. Oceanogr.,* **1,** 241–248.

Hsieh, W. W., M. K. Davey, and R. C. Wajsowicz, 1983: The free Kelvin wave in finite-difference numerical models. *J. Phys. Oceanogr.,* **13,** 1383–1397.

Kalnay, E., and Coauthors, 1996: The NCEP/NCAR 40-Year Reanalysis Project. *Bull. Amer. Meteor. Soc.,* **77,** 437–471.

Kelly, K. A., M. J. Caruso, and J. A. Austin, 1993: Wind-forced variations in sea surface height in the northeast Pacific Ocean. *J. Phys. Oceanogr.,* **23,** 2392–2411.

Killworth, P. D., D. B. Chelton, and R. A. de Szoeke, 1997: The speed of observed and theoretical long extratropical planetary waves. *J. Phys. Oceanogr.,* **27,** 1946–1966.

Lagerloef, G. S. E., 1995: Interdecadal variations in the Alaska gyre. *J. Phys. Oceanogr.,* **25,** 2242–2258.

Large, W. G., and S. Pond, 1982: Sensible and latent heat flux measurements over the ocean. *J. Phys. Oceanogr.,* **12,** 464–482.

——, J. C. McWilliams, and S. C. Doney, 1994: Oceanic vertical mixing: A review and a model with a nonlocal boundary layer parameterization. *Rev. Geophys.,* **32,** 363–403.

——, G. Danabasoglu, and S. C. Doney, 1997: Sensitivity to surface forcing and boundary-layer mixing in a global ocean model: Annual mean climatology. *J. Phys. Oceanogr.,* **27,** 2418–2447.

——, J. C. McWilliams, P. R. Gent, and F. O. Bryan, 2001: Equa-

torial circulation of a global ocean climate model with anisotropic horizontal viscosity. *J. Phys. Oceanogr.,* **31,** 518–536.

Mantua, N. J., S. R. Hare, Y. Zhang, J. M. Wallace, and R. Francis, 1997: A Pacific interdecadal climate oscillation with impacts on salmon production. *Bull. Amer. Meteor. Soc.,* **78,** 1069–1079.

Miller, A. J., D. R. Cayan, T. P. Barnett, N. E. Graham, and J. M. Oberhuber, 1994: Interdecadal variability of the Pacific Ocean: Model response to observed heat flux and wind stress anomalies. *Climate Dyn.,* **9,** 287–302.

Musgrave, D. L., T. J. Weingartner, and T. C. Royer, 1992: Circulation and hydrography of the northwestern Gulf of Alaska. *Deep-Sea Res.,* **39,** 1499–1519.

Pedlosky, J., 1996: *Ocean Circulation Theory*. Springer-Verlag, 453 pp.

Polovina, J. J., G. T. Mitchum, and G. T. Evans, 1995: Decadal and basin-scale variation in mixed-layer depth and the impact on biological production in the central and North Pacific, 1960–88. *Deep-Sea Res.,* **42,** 1701–1716.

Qiu, B., 2002: Large-scale variability in the midlatitude subtropical and subpolar North Pacific Ocean: Observations and causes. *J. Phys. Oceanogr.,* **32,** 353–375.

Reed, R. K., R. D. Muench, and J. D. Schumacher, 1980: On the baroclinic transport of the Alaskan Stream near Kodiak Island. *Deep-Sea Res.,* **27A,** 509–523.

Royer, T. C., 1981: Baroclinic transport in the Gulf of Alaska. Part I: Seasonal variations of the Alaska Current. *J. Mar. Res.,* **39,** 239–250.

Sverdrup, H. U., 1947: Wind-driven currents in a baroclinic ocean with application to the equatorial currents of the eastern Pacific. *Proc. Natl. Acad. Sci.,* **33,** 318–326.